

Review

Review of Selected Advances in Electrical Capacitance Volume Tomography for Multiphase Flow Monitoring

Rafiu K. Rasel ¹, Shah M. Chowdhury ¹, Qussai M. Marashdeh ² and Fernando L. Teixeira ^{1,*}

¹ ElectroScience Laboratory, Department of Electrical and Computer Engineering, The Ohio State University, Columbus, OH 43212, USA; rasel.1@osu.edu (R.K.R.); chowdhury.79@osu.edu (S.M.C.)

² Tech4Imaging LLC, Columbus, OH 43220, USA; marashdeh@tech4imaging.com

* Correspondence: teixeira.5@osu.edu

Abstract: Electrical Capacitance Volume Tomography (ECVT) has emerged as an attractive technology for addressing instrumentation requirements in various energy-related multiphase flow systems. ECVT can monitor multiple flow conditions and reconstruct real-time 3D images from capacitance measurements using a large set of electrode plates placed around the processes column enclosing the sensed flow system. ECVT is non-intrusive and allows the measurement of changes in mutual capacitance between all possible plate pair combinations. The objective of this paper is to provide a comprehensive review of recent advances in ECVT, enabling robust monitoring of multiphase flows, especially water-containing multiphase flows.

Keywords: electrical capacitance volume tomography; image reconstruction; multiphase flow; flow velocimetry; flow monitoring; machine learning



Citation: Rasel, R.K.; Choudhury, S.M.; Marashdeh, Q.M.; Teixeira, F.L. Review of Selected Advances in Electrical Capacitance Volume Tomography for Multiphase Flow Monitoring. *Energies* **2022**, *15*, 5285. <https://doi.org/10.3390/en15145285>

Academic Editor: Bjørn H. Hjertager

Received: 25 June 2022

Accepted: 18 July 2022

Published: 21 July 2022

Publisher's Note: MDPI stays neutral with regard to jurisdictional claims in published maps and institutional affiliations.



Copyright: © 2022 by the authors. Licensee MDPI, Basel, Switzerland. This article is an open access article distributed under the terms and conditions of the Creative Commons Attribution (CC BY) license (<https://creativecommons.org/licenses/by/4.0/>).

1. Introduction

Next-generation power and energy systems will require greater flexibility in their operations to meet higher efficiency and lower emission standards, geared toward simultaneously meeting consumer demand and adhering to increased environmental and associated regulatory constraints. Advanced sensors that can accurately measure flow rates and various phase hold-up information of multi-phase flow systems are of great importance for optimizing and controlling diverse energy generation processes [1–8]. However, the availability of such sensors, particularly at high temperatures and pressures, is presently quite limited.

Electrical Capacitance Tomography (ECT), and more recently, Electrical Capacitance Volume Tomography (ECVT), have emerged as attractive technologies for addressing instrumentation requirements in various energy-related multi-phase flow systems [9–14]. Energy industry requirements necessitate the acquisition of real-time data from critical locations along the energy supply chain where harsh operational conditions may exist. Real-time data from such locations are highly valuable, for example, for power plant operators to adequately monitor and control fuel feeding rate and the combustion process. ECVT in particular, with its three-dimensional (3D) imaging capability, can visualize multiple flow conditions and variables such as concentration, velocity, temperature, and composition in hard-to-reach locations. ECVT reconstructs 3D real-time images from capacitance measurements using a large set of electrode plates placed around the processes column enclosing the sensed flow system [15,16]. ECT and ECVT are non-intrusive and allow the measurement of changes in mutual capacitance between all possible plate pair combinations. These capacitance changes stem from variations in the dielectric properties of different species within the imaging domain. Such variations can be caused by a change in phase concentration in a reacting system (i.e., multi-phase flow), a temperature variation in reacting components (i.e., hot unit flows), or a change in chemical composition (i.e.,

ionization in flames). In ECVT, an image reconstruction algorithm maps back changes in electrical capacitance into a 3D visualization of the underlying process flow.

The nature of energy processes and their often harsh environments limits the number of available approaches to address sensor and instrumentation needs. ECT and ECVT are unique in that they can be adapted to harsh conditions while retaining advantages in terms of safety, fast imaging speeds, immunity to noise, scalability to industrial sizes, flexibility for imaging complex geometries, and relatively low operational cost. Due to these advantages, much research has been done in recent years to improve ECT and ECVT for monitoring multiphase flows [15–23]. The objective of this paper is to provide a summary review of selected research advances in ECT and ECVT sensor technology for monitoring and imaging multiphase flows, including water-containing multiphase flows.

2. Electrical Capacitance Volume Tomography

2.1. Forward Problem

Generally speaking, the image reconstruction problem in ECVT consists of two main problems, viz., the forward problem and the inverse problem. The objective of the forward problem in ECVT is to accurately model the measurement process, i.e., to obtain the capacitance data from a given permittivity distribution $\varepsilon(x, y, z)$ from the volume of interest (VoI), and the inverse problem seeks to reconstruct the $\varepsilon(x, y, z)$ in the VoI from the measured capacitance data. Figure 1 illustrates a schematic representation of a typical ECVT setup consisting of an ECVT sensor, a data acquisition system, and a data visualization tool (e.g., a computational device). Figure 2 shows the photograph of a data acquisition system together with ECVT sensors of various sizes and with different numbers of electrode channels.

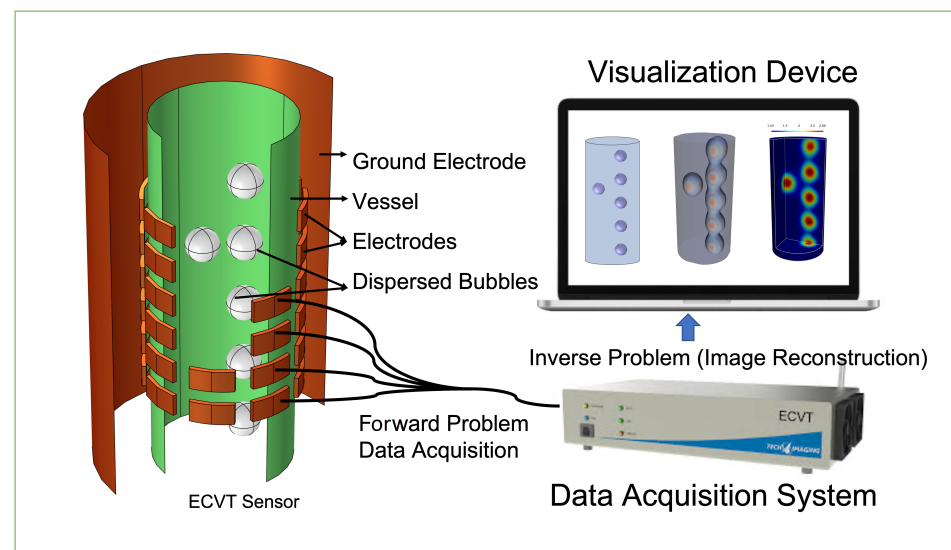


Figure 1. Schematic representation of an ECVT setup used in multiphase flow monitoring.

The discrete form of the forward problem under the Born (linear) approximation can be expressed as [12,17–23]:

$$c = Sg \quad (1)$$

where c is an $M \times 1$ mutual capacitance vector, g is an $N \times 1$ permittivity distribution vector, and S is an $M \times N$ sensitivity (Jacobian) matrix [17–19,24–26]. The mutual capacitance between a given electrode pair (i, j) is measured by applying a time-harmonic (AC) voltage to electrode i while the remaining electrodes $j \neq i$ are grounded. The resulting current is then measured in all remaining electrodes j to obtain the resulting admittance data between (i, j) . This procedure is repeated by activating each electrode separately to obtain all possible independent mutual capacitance measurements. If the total number of electrodes is N , there will be a total of $M = n(n - 1)/2$ independent admittance (or mutual capacitance) measurements.



Figure 2. Data acquisition system and several cylindrical ECVT sensors of various sizes and with different numbers of electrode channels.

2.2. Inverse Problem

Formally, the solution to Equation (1) could be written as $g = S^{-1}c$; however, S is severely underdetermined (e.g., $M \ll N$), and a direct inverse of S does not exist. Additionally, the inverse problem in Equation (1) is ill-posed (there is no unique solution) and ill-conditioned; i.e., small changes in c (due to measurement noise for example) might lead to larger discrepancies in g . Therefore, obtaining a meaningful inverse problem solution is often challenging. In practice, there are two primary classes of methods to solve the inverse problem: (i) direct methods and (ii) iterative methods [22]. In what follows, this section will describe some of the most commonly adopted methods for ECT and ECVT.

2.2.1. Linear Back-Projection

Linear back projection (LBP), one of the first methods developed for ECT [17,18], is the simplest and fastest approximate solution to Equation (1). The LBP approximation method consists of using the transpose of the sensitivity matrix (S^T , a crude estimation of S^{-1}) to linearly map the permittivity distribution to the measured capacitance data. LBP for Equation (1) can be written as:

$$g = S^T c \quad (2)$$

Figure 3a shows LBP reconstruction of air bubbles dispersed in oil. Reconstruction results are obtained from finite element simulations of a cross-section of air and oil flow using a 12-electrode ECT sensor. The gap between each electrode along the azimuth direction is 7.5 degrees. The inner and outer radii of the vessel holding the flow are 13.5 and 15 cm, respectively. The permittivity of the vessel wall was set to 3, and the permittivity of air and oil set were to 1 and 3, with no conductivity, respectively. The exact size and location of air bubbles are shown using black circles in the reconstructed images. From the figure, it is clear that the images obtained using LBP are of low resolution and only provide rough qualitative information [3].

2.2.2. Pseudo-Inverse with Tikhonov Regularization

Although LBP reconstruction provides good qualitative results, in practice, a better image reconstruction algorithm is desired to obtain superior quantitative information about the VoI. Since S is underdetermined, an approximate solution to Equation (1) in the least square sense can be expressed in terms of the Penrose pseudo-inverse matrix as:

$$g = (SS^T)^{-1}S^T c \quad (3)$$

However, since S is severely ill-conditioned and ill-posed, the inverse of (SS^T) may be singular in most cases. Regularization techniques have been developed to solve ill-posed and ill-conditioned inverse problems, and Tikhonov Regularization (TR) is commonly used to solve such inverse problems. TR is a robust algorithm for inverse problems, and depending on the flows, it can be a powerful/efficient tool to solve ECT reconstruction problems. Based on the TR procedure, an approximate solution for g can be written as:

$$g = (SS^T + \mu I)^{-1} S^T c \quad (4)$$

where μ is the regularization parameter and I is the identity matrix. Figure 3b shows TR reconstruction of air bubbles dispersed in oil. From the figure, it is clear that compared to LBP, the TR algorithm provides better resolution. However, the performance of the TR algorithm is highly dependent on the regularization parameter μ , and the best choice is problem-dependent. As a result, the TR algorithm is not always suitable for highly dynamic flow scenarios.

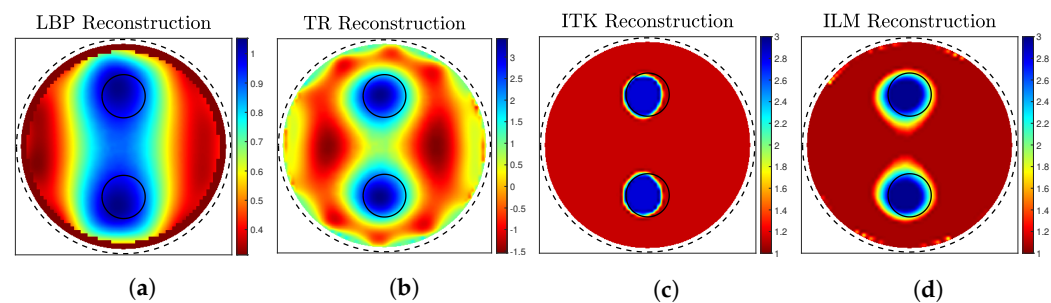


Figure 3. The reconstructed images of air bubbles dispersed in oil. The exact sizes and locations of air bubbles are shown using black circles in the reconstructed images. Images were obtained using (a) LBP, (b) unprojected TR, (c) ITR, and (d) ILM reconstruction algorithms, respectively.

2.2.3. Iterative Tikhonov Regularization

The imaging problem in ECVT is often highly nonlinear, and it is difficult to obtain an accurate reconstruction directly based on the linearized inverse problem as a direct method. Iterative methods are often used to obtain robust results for such an ill-posed and ill-conditioned nonlinear inverse problem [22]. Based on the Tikhonov Regularization, Iterative Tikhonov Regularization (ITR) can be used to obtain better image reconstruction results for the ECVT problem. The ITR method for Equation (1) is expressed as:

$$g_{k+1} = g_k - (SS^T + \mu I)^{-1} S^T (Sg_k - c) \quad (5)$$

where k is the number of iterations. This ITR implementation is a *local* linear representation of the non-linear ITR method. Similar to direct TR, the reconstruction quality also depends on the regularization parameter μ . Figure 3c shows ITR reconstruction of air bubbles dispersed in oil. The reconstruction quality is superior to all the methods discussed in this section. However, as noted, the final reconstruction quality is a function of μ , and the value of μ can depend on several factors. Additionally, since a minor change in μ can lead to a higher reconstruction error, ITR is not always suitable for highly dynamic flow scenarios.

2.2.4. Iterative Landweber Method

The Iterative Landweber Method (ILM) is one of the most popular methods used in the ECVT reconstruction problem [27–29]. The ILM solution to Equation (1) can be expressed as:

$$g_{k+1} = g_k - \alpha_k S^T (Sg_k - c) \quad (6)$$

where α_k is the penalty factor of iteration k . The optimal value of α_k depends on several factors such as flow type (bubbly, columnar, stratified, etc.) and the permittivity of the

materials inside the VoI. The value of α_k can be a fixed quantity, or it can be chosen optimally for each iteration k . For example [29]:

$$\alpha_k = \frac{\|\mathbf{S}^T(\mathbf{S}\mathbf{g}_k - \mathbf{c})\|}{\|\mathbf{S}\mathbf{S}^T(\mathbf{S}\mathbf{g}_k - \mathbf{c})\|}. \quad (7)$$

where $\|\cdot\|$ is the 2-norm. Figure 3d shows ILM reconstruction of air bubbles dispersed in oil. Although the ITR reconstruction result presented in the figure is superior, the reconstruction quality is dependent upon μ , and the optimal value of μ might be difficult to determine a priori. On the other hand, the ILM algorithm does not suffer from such limitations.

2.2.5. Non-Traditional Reconstruction Algorithms

Although ILM is a robust method for ECVT reconstruction, there are still some issues with the ILM approach. For example, since the problem is ill-posed, the ILM method is semi-convergent (i.e., it initially converges, but it may start to diverge after a certain number of iterations), and the optimal iteration number (i.e., exhibiting the minimum error) needs to be determined using a trial and error approach. Moreover, the resolution of reconstructed flow is often limited by the size of dispersed phases, the number of dispersed phases present in VoI and the location of each dispersed phase in the VoI, and the flow type.

To overcome these limitations, several image reconstruction algorithms have been studied [30–33] promising robust ECVT reconstruction compared to ILM. For example, Ye et al. [31] proposed an algorithm based on the sparse representation of the sensitivity matrix and the capacitance vector. The sparse representations are obtained using a suitable mapping on the base model. The reconstructed images show improved results compared to ILM; however, the algorithm is computationally expensive, and in many cases, ILM may provide comparable results. Soleimani et al. [33] proposed a non-linear implementation of the ITR method. Although the results presented in [33] show promise, using a non-linear forward solver is computationally expensive and still impractical to implement for real-time industrial imaging scenarios. In addition to those approaches, machine learning-based algorithms have also been considered recently. These algorithms will be discussed separately later in this paper.

2.3. Sensitivity Matrix Computation

There are several works that provide guidelines for generating a sensitivity matrix for ECVT [17–20,25,26]. The most popular method with which to generate a sensitivity matrix for ECVT is based on the definition of Jacobian matrix between \mathbf{c} and \mathbf{g} [9,17–19,24]. Typically, the elements of the sensitivity matrix $S_{ij}(p = (x, y, z))$ for the p th voxel between electrode pair (i, j) can be approximated by:

$$S_{ij}(p) = \frac{1}{V_i V_j} \int_p \vec{E}_i(p) \cdot \vec{E}_j(p) d\Omega \quad (8)$$

where $d\Omega$ is a infinitesimal volume element; $\vec{E}_i(p)$ and $\vec{E}_j(p)$ are the electric fields at voxel p when only the i th or only the j th electrode is excited, respectively; and all remaining electrodes are grounded. V_i and V_j are the voltages applied to electrode i and electrode j , respectively. For ECVT problems, these fields can be obtained with a variety of methods, such as a 3D finite element or finite-difference solvers.

2.4. Selected Open Challenges

In soft-field tomography such as ECVT, the smallest feature that can be extracted is correlated with the electrode size used in measurements. Although reducing the size of individual electrodes, in theory, can improve imaging resolution to some extent, an arbitrary decrease in electrode size will not result in a proportional improvement in imaging resolution. Figure 4 shows the reconstructed images of a few small oil bubbles dispersed in air obtained using a simulation with 24-electrode and 48-electrode ECT sensors. The total span of the electrodes along the azimuth in both cases was 75% of the circumference of the vessel (with the remaining 25% comprising the gaps between electrodes). The outer and inner diameters of the vessel were 15 and 13.5 cm, respectively. The areas of the circular bubbles dispersed in air were 1%, 0.5%, and 0.1% of the total cross-sectional area of the region of interest (RoI), respectively. Images were obtained using ILM after 10,000 iterations. The reconstructed images of the large and smaller bubbles are almost identical for both 24 and 48-electrode ECT sensors. Figure 5 shows that when multiple small bubbles are grouped close together, ECT cannot distinctly separate them. From Figure 4, one can infer that the smallest feature ECT can theoretically extract is roughly 0.5% area of the RoI. In practice, this rough estimate might vary according to several additional factors, such as the number of bubbles, the location of each bubble (the ECT resolution tends to decrease towards the center of the RoI), and the signal-to-noise ratio (SNR) of the measurements.

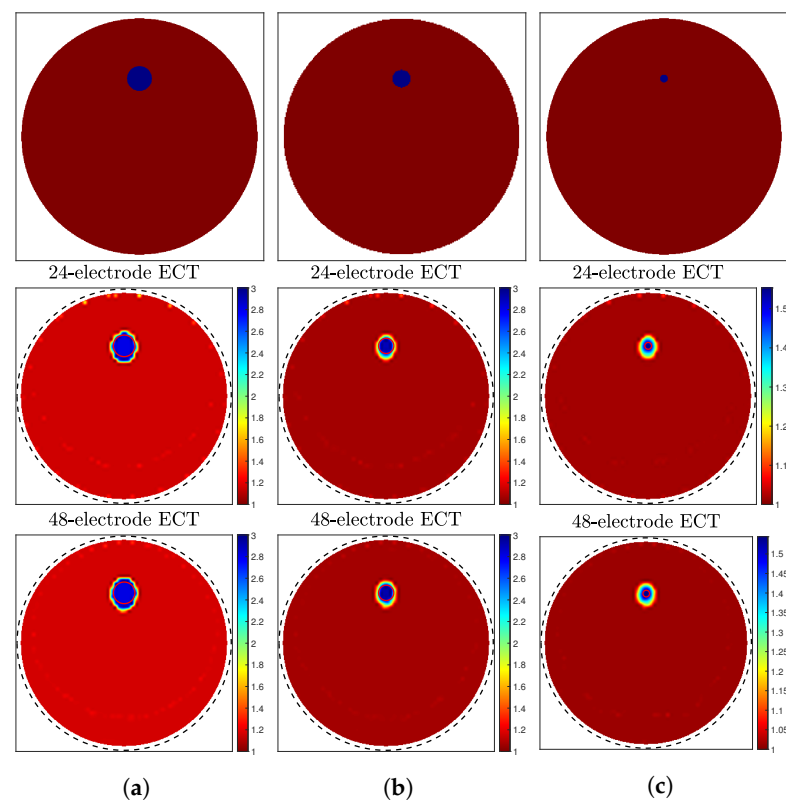


Figure 4. Illustration of ECT image reconstruction of small objects. The top images show the true distribution. The middle and bottom images show reconstructed images obtained using ILM with 24-electrode and 48-electrode ECT systems. The respective areas of the object of interest in the figures are (a) 1%, (b) 0.5%, and (c) 0.1% of the RoI, respectively.

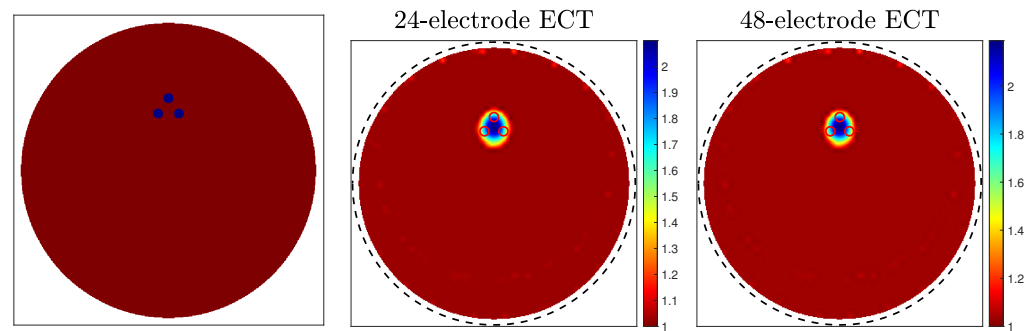


Figure 5. Example considering three very small objects of size below the ECT resolution limit. The leftmost plot shows the ground truth. The middle and right plots show the image reconstruction based on ILM with 24 and 48 electrode sensors, which is nearly identical. ECT cannot individually reconstruct the very small individual objects in this case; rather, it provides a region of interest where the objects reside.

3. Simultaneous Permittivity/Conductivity ECVT-Based Reconstruction

Industrial multiphase flows containing water can be complex, and traditional ECVT might fail to provide good results if the flow is water-continuous (i.e., with water corresponding to the continuous phase). There are several methods based on the use of electrical impedance tomography (EIT) sensors to image water-continuous flows. However, EIT requires galvanic contact between the flow and the electrodes to work optimally. This intrusive EIT property makes it undesirable and impractical in many industrial applications. Therefore, to monitor complicated water-continuous multiphase flows, Marashdeh et al. [34,35] developed a multimodal imaging system where the existing ECVT sensor system is used to simultaneously monitor variations in the capacitance and the dissipated power within the VoI (which maps to the permittivity and conductivity distributions inside the VoI, respectively). The proposed monitoring technique utilizes the measurement of the real and imaginary parts of the complex-valued admittance $Y = G + jB$ as measured by a standard ECT sensor (Figure 2). The imaginary part of Y or susceptance B maps to the capacitance data to monitor the *permittivity* distribution as before, and the real part of Y or the conductance G maps to the power dissipation data to monitor the *conductivity* distribution in the VoI. The proposed image reconstruction technique involves the use of two capacitance/power sensitivity matrices in tandem. Under a linear Born approximation, the forward problem can be expressed similarly as before, and traditional image reconstruction algorithms such as ILM can be used as reconstruction tools [34,35]. Zhang et al. [36] in their work also proposed a method based on the multifrequency excitation of the ECT sensor to simultaneously monitor permittivity and conductivity distribution. The method by Zhang et al. utilizes complex admittance paired with a complex sensitivity matrix to reconstruct the permittivity and the conductivity distribution. However, due to the complex representation of the forward and inverse problem, the problem is computationally expensive to solve.

4. Displacement Current Phase Tomography

As noted before, when monitoring water-containing multiphase flows, the use of conventional EIT is undesired due to the need for galvanic contact. In addition, the application of multimodal ECVT sensors proposed by Marashdeh et al. [34,35] and Zhang et al. [36], discussed in the previous section, can increase the implementation's complexity. Therefore, it is highly desirable to develop a robust water-containing flow monitoring algorithm that is not necessarily intrusive to the flow. Gunes et al. [37] developed a new imaging modality exploiting the same ECVT hardware and image reconstruction algorithm to monitor water-containing flows named Displacement Current Phase Tomography (DCPT). Similarly to ECVT, the analysis and application of DCPT sensors can be separated into two problems. The direct or forward problem in DCPT measures or models the (complex-valued) admittance Y data from a given electric conductivity distribution $\sigma(x, y, z)$ inside

the VoI. In the inverse problem, $\sigma(x, y, z)$ is treated as an unknown property in the VoI and reconstructed from the small-angle perturbation in the phase of admittance. Under a linear (Born) approximation of the forward problem, DCPT can be expressed as:

$$\boldsymbol{\phi} = \mathbf{S}_d \boldsymbol{q} \quad (9)$$

where $\boldsymbol{\phi}$ is an $M \times 1$ column vector encoding the phase of the complex-valued admittance measured between each electrode pair, \boldsymbol{q} is a $N \times 1$ column vector encoding the volumetric $\sigma(x, y, z)$ distribution, and \mathbf{S}_d is a $M \times N$ sensitivity (Jacobian) matrix. One of the advantages of using DCPT over multimodal application of ECT proposed by Qussai et al. [34,35] and Zheng et al. [36] is that, under linear approximation, the sensitivity matrices of ECT/ECVT and DCPT are identical; i.e., $\mathbf{S}_d = \mathbf{S}$ [37]. Moreover, the same image reconstruction techniques developed for ECT/ECVT can be used for DCPT as well. In practice, DCPT implementation is nearly identical to ECVT, the main difference being that the imaginary (capacitive) part $\Im m(Y)$ of the measured admittance data is utilized in ECVT, whereas DCPT utilizes the admittance *phase*. Moreover, data normalization techniques used in DCPT differ slightly from those used in ECVT. Further details on DCPT can be found in [37].

5. Maxwell–Wagner–Sillars Effect in ECVT Applications

Although DCPT is robust for water-continuous flows, ECVT tends to be superior for water dispersed flows. As stressed in the preceding sections of this paper, the image reconstruction problem in ECVT is challenging for several reasons. The presence of water makes it even more challenging because of the large permittivity of water and the ensuing stronger nonlinearity of the inverse problem. However, due to the presence of a conducting phase (water), water-containing flows may yield Maxwell–Wagner–Sillars (MWS) polarization. The MWS polarization (Figure 6) is a consequence of the surface migration of charges at the interface between media when at least one of the media is conducting and/or lossy [38–40] (such as water). This polarization effect was first discovered by Maxwell [40–42], and it was later studied and further analyzed by Wagner and Sillars [43]. Depending on the dispersed phase properties (e.g., inclusion shapes and sizes, and homogeneous or inhomogeneous dispersion), the extent and characteristics of the MWS effect will vary. Among the mixture formulas developed for dielectric mixtures, Hanai’s formula for complex-valued dielectric permittivities provides the best estimation for spherically dispersed homogeneous mixtures [38,40,44,45], a type of mixture that approximates well a vast number of practical scenarios. Hanai’s formula for a complex dielectric constant is written as [45]

$$\left(\frac{\varepsilon_d^* - \varepsilon_c^*}{\varepsilon_d^* - \varepsilon_m^*} \right)^3 \frac{\varepsilon_m^*}{\varepsilon_c^*} = \frac{1}{(1 - \varphi)^3} \quad (10)$$

where ε_d^* , ε_c^* , and ε_m^* are the complex permittivities of the dispersed phase, continuous phase, and mixture, respectively; and φ is the volume fraction of the dispersed phase. The complex permittivity ε^* of a medium can be written in terms of permittivity ε and effective conductivity σ as $\varepsilon^* = \varepsilon - j\sigma/(\omega\varepsilon_0)$, where ω is the frequency and ε_0 is the free-space permittivity.

5.1. MWS-ECT Imaging of Water-Containing Flows

Recently, Rasel et al. [38,39] proposed a method exploiting MWS polarization to continuously monitor water-containing non-homogeneous flows (e.g., bubbly, slug vertical, annular, core, and columnar). The proposed algorithm exploits the fact that measurements obtained at distinct frequencies will carry slightly different information due to different MWS polarization effects at those frequencies. The resulting measurement difference due to MWS polarization at two frequencies ω_1 and ω_2 can be combined as [38,39]:

$$\mathbf{c}^{md} = \mathbf{c}_{\omega_2}^m - \lambda \mathbf{c}_{\omega_1}^m, \quad (11)$$

where λ is an MWS factor, and \mathbf{c}^{md} is the measurement vector related to the conducting (lossy) phase(s) responsible for the MWS polarization [38,39].

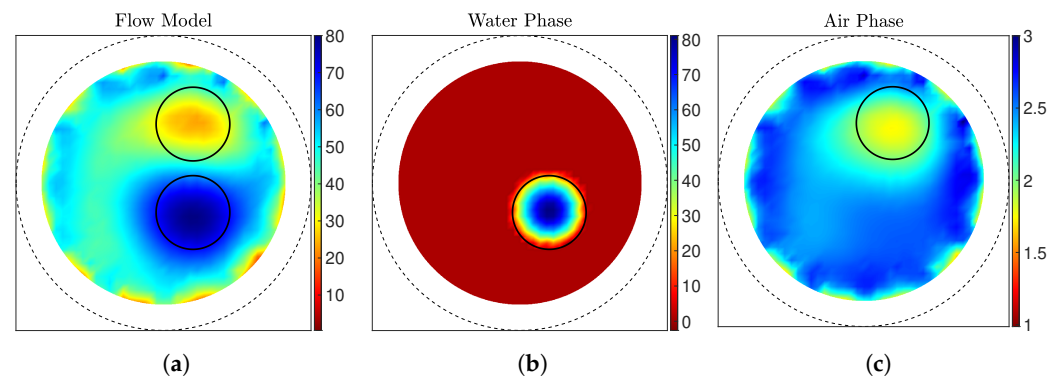


Figure 6. Reconstructed images from simulations of air and water bubbles dispersed in oil. (a) Reconstructed flow model obtained using ECT, (b) MWS-ECT reconstructed image of water, (c) MWS-ECT reconstructed image of air. Details of the simulation can be found in [38].

After obtaining the capacitance vector related to the conducting phase, the capacitance vector related to the nonconducting phase(s) is derived as $\mathbf{c}^{mn} = \mathbf{c}_{\omega_2}^m - \gamma \mathbf{c}_{\omega_1}^m$, where \mathbf{c}^{mn} is the capacitance vector related to the nonconducting phases, and γ is a properly chosen weight discussed in [38]. After obtaining \mathbf{c}^{md} and \mathbf{c}^{mn} , any image reconstruction tool available for the conventional ECT/ECVT imaging will be sufficient to generate images of both the conducting and nonconducting phases. Figure 6 shows the reconstructed images of a region of interest (RoI) obtained using the regular ECT and the MWS-ECT. Figure 7 shows the reconstructed images of a three-phase water-dispersed flow. The actual size and location of dispersed phases are shown using black circles in the figure. It is clear from the reconstructed images presented in Figure 6 that MWS-ECT can separately image both the conducting and the nonconducting phase(s) with better resolution than traditional ECT [38,39]. We should note that a recent related work by Hossain et al. [46] reports a three-phase flow decomposition method based on single-frequency measurements; however, it requires a priori knowledge of the permittivity values of each phase. The application of MWS-ECT in experimental settings is a straightforward process. For MWS-ECT, water-containing flow measurements should be obtained at two distinct frequencies using the data acquisition hardware. After acquiring all the relevant measurements, the capacitance vector related to the conducting and non-conducting phases can be extracted using the method outlined here. Afterward, any image reconstruction algorithm available for ECT can be used for MWS-ECT image reconstruction.

5.2. Volume Fraction Estimation in Homogenized Water-Containing Flows

Not all industrial water-containing flows are non-homogeneous. If the flow is homogenized, the MWS-ECT imaging techniques developed for non-homogeneous flow will be insufficient to provide meaningful volume information in the VoI. Recently, Rasel et al. [47,48] proposed a method based on the low-frequency estimation of MWS polarization to estimate volume fractions of each phase of a homogeneously dispersed water-containing flow.

Although Hanai's formula can provide volume fractions of both phases for a two-phase water-containing mixture (flow), the electrical properties (i.e., permittivity and conductivity) of all phases must be known a priori. The low-frequency estimation of the MWS effect, however, can simplify the volume calculation problem as detailed in [47]. The low-frequency estimation of water-dispersed flow can be expressed as [40,47]:

$$\varphi_d = 1 - \left(\frac{\epsilon_c}{\epsilon_m} \right)^{1/3} \quad (12)$$

$$\varphi_d = 1 - \left(\frac{\sigma_c}{\sigma_m} \right)^{1/3} \quad (13)$$

where φ_d is the volume fraction of the dispersed phase. The low-frequency estimation for the water-continuous flow can be expressed as [40,47]:

$$\varphi_c = \left(\frac{\epsilon_m}{\epsilon_c} \right)^{2/3} \quad (14)$$

$$\varphi_c = \left(\frac{\sigma_m}{\sigma_c} \right)^{2/3} \quad (15)$$

Figure 7 shows a comparison of the actual versus calculated water volume fraction obtained from a flow loop experiment with homogenized two-phase water-containing flows. Further details of the experiment are provided in [48].

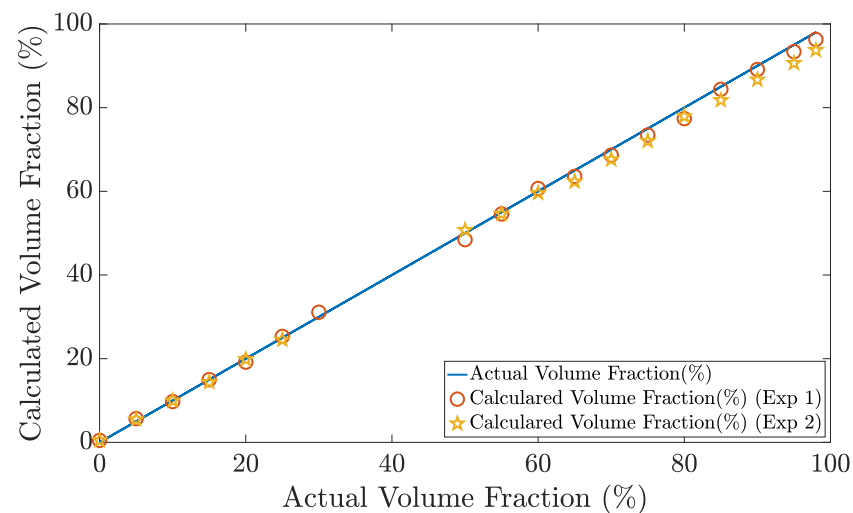


Figure 7. Calculated versus actual volume fractions of water obtained from two-phase oil-water flows based on controlled flow loop experimental data. Details of the experimental setup can be found in [48].

In an experimental setup, the measured admittance data Y contain the necessary encoding of the permittivity and conductivity for use by the method outlined in this section. Preliminary studies presented in [47,48] demonstrate that for water-dispersed flow, Equation (12), and for water-continuous flow, Equation (15), provide adequate approximations. In terms of the measured data Y , the relations can be expressed as:

$$\varphi_d = 1 - \left[\frac{\Im m(1/Y_m)}{\Im m(1/Y_c)} \right]^{1/3} \quad (16)$$

$$\varphi_c = \left[\frac{\Re e(1/Y_c)}{\Re e(1/Y_m)} \right]^{2/3} \quad (17)$$

where Y_m and Y_c are the measured data when the vessel is filled with the two-phase homogeneous emulsion (mixture) to be analyzed and with the continuous phase only, respectively. A more detailed discussion on this can be found in [47].

5.3. MWS-DCPT

Although DCPT is robust compared to ECVT for water-continuous flows, the image resolution of DCPT is poorer in quality. To improve the resolution of DCPT-based imaging modality, a multifrequency MWS-DCPT exploiting the MWS effect was proposed in [49].

Generally speaking, DCPT image reconstructions are generated from measurements obtained at a single frequency. The multifrequency MWS-DCPT method proposed in [49] utilizes a frequency sweep to obtain measurement at different frequencies and again exploits the difference in measured data due to MWS polarization to improve imaging resolution. Assuming $\bar{\phi}_\omega^m$ is the measured phase obtained at frequency ω , the proposed method exploits the difference of MWS polarization measured at two different frequencies $\omega_1 > \omega_2$ as follows [49]

$$\bar{\phi}^d = (\bar{\phi}_{\omega_1}^m - \bar{\phi}_{\omega_1}^f) - \lambda(\bar{\phi}_{\omega_2}^m - \bar{\phi}_{\omega_2}^f), \quad (18)$$

where λ is a parameter that can be calculated using the least square method [49], $\bar{\phi}_\omega^f$ is the measured phase when the vessel is filled with conducting continuous phase (water) at frequency ω , and $\bar{\phi}_\omega^m$ is the measured phase with the multiphase flow. After obtaining $\bar{\phi}^d$, it can be used in Equation (9) (e.g., $\bar{\phi}^d = S_d q$) to obtain an improved image of the flow. Figure 8 shows the reconstructed images of air bubbles dispersed in water obtained using MWS-DCPT and conventional DCPT reconstruction. This figure shows that MWS-DCPT can improve DCPT image reconstruction performance.

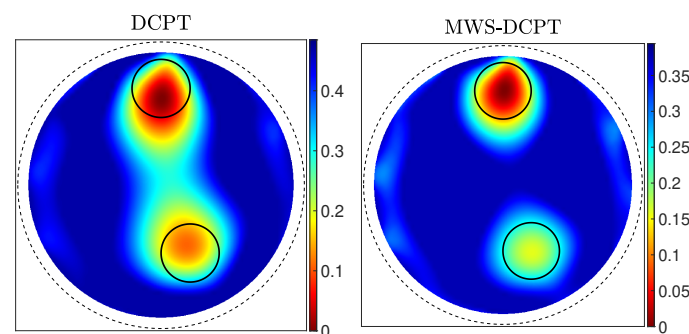


Figure 8. Reconstructed image of air bubbles dispersed in oil. The admittance data for the reconstruction were obtained using finite element simulations. Further details can be found in [49].

6. Adaptive ECVT

In principle, it is reasonable to expect that an increase in the number of active electrodes may enhance the imaging resolution of ECVT because of added measurement information. However, there are certain fundamental limitations to this strategy. For example, the Laplacian (harmonic) nature of the interrogating electric field leads to increasingly correlated data among many electrode combinations, especially while imaging the center of the VoI. In addition, the presence of measurement noise and the need for a minimum SNR prevent an arbitrary decrease in the electrode area (to increase the number of electrodes and hence the number of measurements by the sensor). Adaptive ECVT (AECVT) seeks to increase the number of independent measurements without actually decreasing the corresponding electrode area [50–56]. AECVT accomplishes this by electronically combining different, individual electrode segments into synthetic electrodes, as illustrated in Figure 9.

As illustrated in Figure 9, synthetic electrode scanning allows the configuration of an $L \times N_L$ electrode (where L is the number of electrode layers and N_L is the number of electrodes in each layer) AECVT system with different $v_s \times h_s$ synthetic electrode configurations. Here, v_s and h_s are the numbers of electrodes segments in the vertical and horizontal directions, respectively, that are combined to form a synthetic electrode. In Figure 9, $v_s = 2$ and $h_s = 2$. Using synthetic electrode scanning, the number of different measurements M_s

for a $L \times N_L$ -electrode AECVT sensor with a $v_s \times h_s$ synthetic electrodes configuration is in general given by:

$$M_s = (L + 1 - v_s) \left(\frac{N_L(N_L - 1)}{2} - N_L(h_s - 1) \right) + (N_L)^2 \frac{(L + 1 - 2v_s)(L + 2 - 2v_s)}{2}. \tag{19}$$

Equation (19) is only valid when $v_s \leq L/2$ and $h_s \leq N_L/2$, which is a typical condition. Ordinarily in AECVT, the multiple segments in a synthetic electrode are excited using the same voltage [50–54]. Nevertheless, as suggested in [53] and as considered in recent studies [55,56], non-uniform voltage excitations within the same synthetic electrode group can be applied as well to provide more control of the interrogating field inside the Vol. Non-rectangular synthetic electrodes can in principle also be considered.

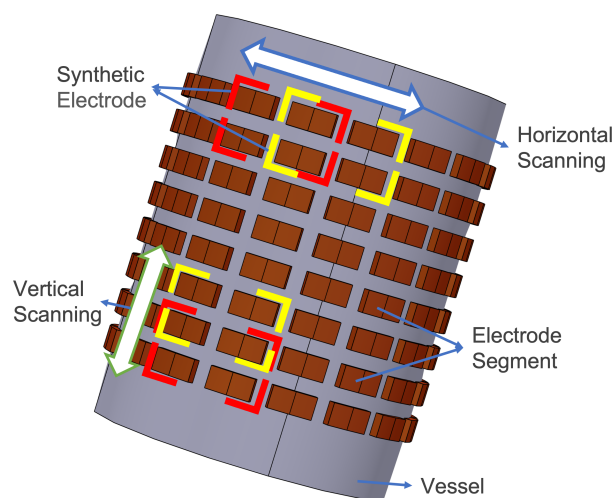


Figure 9. Illustration of an adaptive ECVT sensor. The segments in brown constitute the physical electrodes surrounding the Vol. The red and yellow indications are synthetic electrodes formed by the electronic combination of individual segments (four segments in this example). Synthetic electrodes can be used to attain the minimum required electrode area for a given SNR requirement while enabling additional measurement data. Importantly, they enable fine-stepped scanning (as indicated by the arrows) to provide better sensing resolution.

Flexible Sensitivity Matrix for AECVT

Although Equation (8) provides a guideline for generating sensitivity matrices for traditional ECVT image reconstruction, such a straight forward approach for AECVT can be very time-consuming and repetitive [52–54]. In light of this, Acero et al. [57] proposed an efficient and flexible method to generate sensitivity matrices for AECVT sensors. The first step of the proposed method is to calculate the electric field for each single electrode segment separately. After obtaining this field data, the corresponding (raw) sensitivity matrix S can be found. After generating this raw sensitivity matrix, the sensitivity matrix for a given AECVT excitation setup S_a can be computed using a combination matrix P [57]:

$$c_a = PSg = S_ag \tag{20}$$

where $c_a = Pc$ are the capacitance data obtained from the AECVT under a given adaptive scheme, and c would be the full measurement vector obtained from AECVT sensor without any adaptive activation scheme [57]. Details on the combination matrix P can be found in [57].

7. Cross-Plane Acquisition Technique for ECVT

It is possible to stack a series of ECT sensors along the axial direction of a vessel and combine their 2D images to form a 3D image. We refer to this approach as 3D-ECT. ECVT differs from 3D-ECT in a fundamental way because ECVT also includes the mutual capacitance data between electrodes located in different planes along the axial direction (cross-plane acquisitions). ECVT is often superior in axial resolution compared to 3D-ECT [58]. However, the number of independent measurements in ECVT is often considerably larger than its 2D and 3D counterpart [58,59]. If convenient for certain types of flows, an ECVT sensor can be easily reduced to 3D-ECT by deactivating some of the capacitance channels. For this reason, ECVT can be considered a more flexible strategy than 3D-ECT.

However, if two electrodes are excessively separated along the axial direction, the SNR of the corresponding channel will tend to become very small, rendering the data unusable. To alleviate this issue, Li et al. [59] proposed a sensing strategy removing all measurements between cross-plane sensors separated by more than two sensor layers. Rasel et al. [58] provided a detailed study on various cross-plane acquisition schemes and some basic guidelines for optimal sensing strategy. For example, removing all measurements separated by two or more electrode layers is optimal for large axial electrode heights; however, if the axial electrode height is reduced, additional cross-layer capacitance data should be used for better axial resolution. Figure 10 illustrates the effectiveness of the cross-plane acquisitions [58]. The ECVT sensor in the simulation consists of 10 layers of 8 electrodes each. More details can be found in [58]. From the figure, it can be seen that the optimized ECVT produces more robust images when compared to full ECVT and 3D-ECT.

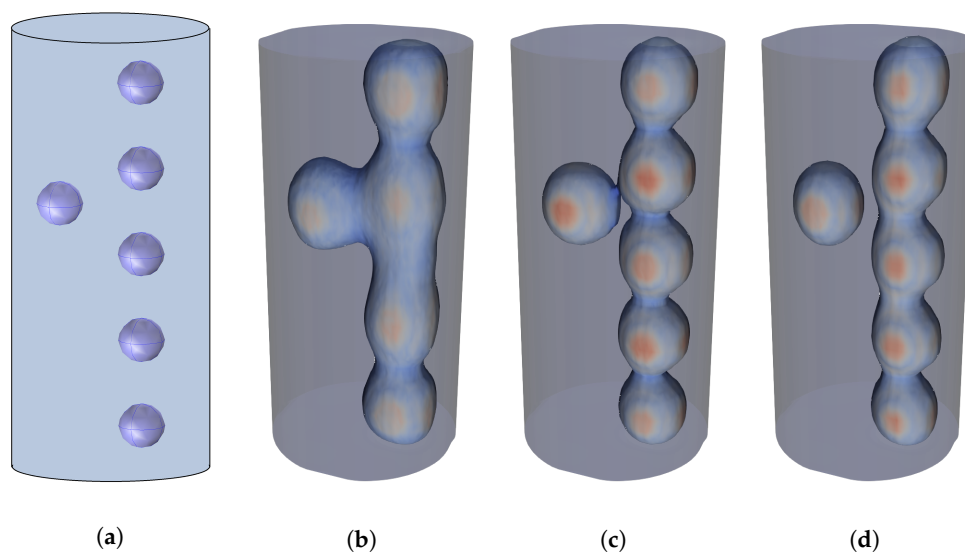


Figure 10. Figure shows the effects of cross-plane optimization in ECVT image reconstruction. (a) Flow model used in the simulation. (b) Reconstructed flow model obtained using 3D-ECT (no cross-plane measurement). (c) Reconstructed flow model obtained using optimal ECVT cross-plane measurements (measurements separated by more than three sensor layers are neglected). (d) Reconstructed flow model obtained using full ECVT measurements. More details of the simulation can be found in [58].

8. ECVT-Based Flow Velocimetry

8.1. Cross-Correlation Based Velocity Calculation

Flow velocimetry is the task of estimating the local velocities of a fluid flow. Of the several measurement tools available for flow velocimetry, many are suboptimal in that they are intrusive to the flow. Given its non-intrusive and non-invasive properties, the application of ECT/ECVT for velocity profiling is of great interest. Several ECT-based methods have been proposed to monitor fluid velocity [60,61]. For example, Warsito et al. [62]

proposed the use of the cross-correlation between images obtained at different times and at different planes along the flow to estimate the 3D velocity of the swarms and bubbles flowing within the flow. Similarly, Saoud et al. [60] proposed a cross-correlation-based technique to monitor the velocities of swirl flow. Another velocimetry approach reported by Botton et al. [63] utilizes a cross-correlation technique based on a simplistic capacitance sensor to reconstruct the axial velocity profile. It achieves good accuracy with the velocity magnitudes; however, it requires improvements with the velocity profile reconstruction.

8.2. Sensitivity Gradient-Based Velocity Calculation

Despite its popularity, the use of cross-correlation often becomes less feasible for 3D velocity profiling due to computational requirements. An alternative method proposed by Chowdhury et al. [64] bypasses the cross-correlation step through a direct velocity to temporal change in capacitance mapping based on the sensor sensitivity gradient, expressed as

$$\frac{\Delta c}{\Delta t} = \left(\mathbf{G}^1 \odot \mathbf{F}_x \right) v_x + \left(\mathbf{G}^1 \odot \mathbf{F}_y \right) v_y + \left(\mathbf{G}^1 \odot \mathbf{F}_z \right) v_z \quad (21)$$

where $\Delta c = c^2 - c^1$ is the change in capacitance between two consecutive frames, Δt is the time difference between two successive frame captures (inverse of the frame rate f_r), (v_x, v_y, v_z) are $N \times 1$ unknown velocity profile vectors, and $(\mathbf{F}_x, \mathbf{F}_y, \mathbf{F}_z)$ are $M \times N$ sensitivity gradient matrices evaluated by taking the gradient of the sensitivity matrix \mathbf{S} . Sensitivity distributions for an opposite electrode pair are shown in Figure 11. The $M \times N$ image matrix \mathbf{G}^1 is defined as $\mathbf{G}^1 = [\hat{g}^1 \ \hat{g}^1 \ \dots \ \hat{g}^1]^T$, where \hat{g}^1 is the reconstructed image corresponding to frame C^1 . Here, \odot denotes element-wise product.

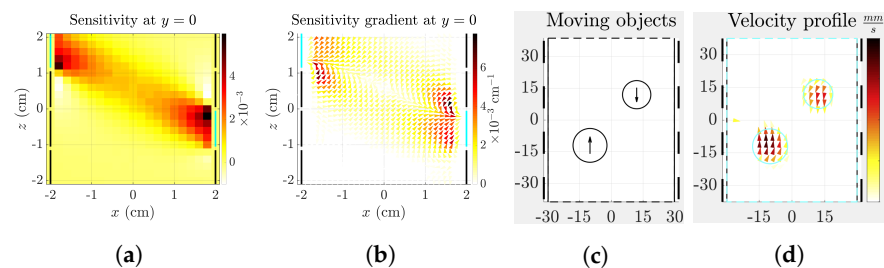


Figure 11. Sensitivity gradient based velocimetry. (a) Sensitivity distribution between a pair of electrodes. (b) Corresponding sensitivity gradient. (c) Simulation setup with moving objects with average velocity of 2 mm/s. (d) Reconstructed velocity profile.

This algorithm enables velocity reconstruction with traditional image reconstruction algorithms. The \mathbf{G}^1 factor acts as a spatial masking on the sensitivity gradient fields, which enables a simple method such as LBP to provide a reasonably good solution. The LBP solution can be optimized for more accurate results as outlined by Park et al. [65] while applying this velocimetry algorithm for a gas–solid flow. Further improvements have included the development of automated stopping criterion for the Landweber iteration method [66]. Velocity reconstruction results based on this algorithm for two moving dielectric objects are shown in Figure 11c,d. This method can be integrated with DCPT to address water-dominated flow velocimetry [67].

A summary description/comparison of the various developments described in this paper is presented in Table 1.

Table 1. Summary description of some selected recent developments in ECT-based and ECVT-based sensing modalities.

Sensing Modality	Reference(s)	Hardware	Objective(s)	Industrial Application(s)	Comments
ECT	[18–20]	ECT	Imaging	Non-conducting multiphase flow imaging and monitoring	Provides cross-sectional image.
ECVT	[9]	ECVT	Imaging, velocimetry, volume fraction estimation	Non-conductive multiphase flow imaging and monitoring	Provides volumetric image.
MWS-ECT	[38,39,47,48]	ECT ECVT	Imaging, volume fraction estimation	Water-Containing flow reconstruction and volume estimation	Allows monitoring of water-containing flows using multifrequency and low-frequency excitations.
DCPT	[37]	ECT ECVT	Imaging	Water-Continuous flow reconstruction and monitoring	Robust for monitoring water-continuous flows compared to traditional ECT.
MWS-DCPT	[49]	ECT ECVT	Imaging	Water-Continuous flow reconstruction and monitoring	Improves imaging resolution of DCPT using multifrequency excitation.
Simultaneous ϵ, σ monitoring	[34–36]	ECT	Imaging	Water-containing flow reconstruction and monitoring	Complex imaging modality compared to MWS-ECT and DCPT.
Cross-plane acquisition optimization	[58,59]	ECVT	Imaging, velocimetry, volume fraction estimation	Multiphase flow monitoring	Reduces computational complexity and improve image quality.
AECVT	[50–56]	ECVT	Imaging, velocimetry, volume fraction estimation	Multiphase flow monitoring	Increases the number of independent measurements without necessarily reducing the effective electrode size.
Velocimetry	[60,61,64,67]	ECVT	Velocity profiling	Multiphase flow transport velocity estimation	Commonly used methods are cross-correlation velocimetry and gradient-based velocimetry.

9. Machine Learning in ECT/ECVT

9.1. ML-Based Flow Characterization

Partial, prior flow characterization can be an important step when monitoring multiphase flows. Specifically, when monitoring water-containing flows, it is highly advantageous to characterize the water-containing flow as either water-continuous or water-dispersed beforehand. For example, Rasel et al. [47] proposed a method to estimate the volume fraction of water in two-phase water-containing flows. However, depending on the state of water in the mixture (i.e., either water-dispersed or water-continuous), a different approach should be selected to perform a good estimation. Machine learning (ML) has proven to be a powerful tool for classification problems. As such, ML tools can be easily adapted to classify and characterize multiphase flows in a robust fashion. Rasel et al. [48] employed a simple feed-forward neural network (NN) with three-hidden layers for initial flow characterization and the same NN model for subsequent volume fraction estimation. The proposed model was shown to achieve high accuracy in classifying water-containing flows and estimating the water-volume fraction from water-containing flows [48].

The type of flow pattern (stratified, annular, core, bubbly, turbulent, mixed, etc.) is other important a priori information. Depending on a specific flow pattern, reconstruction algorithm can be optimized to provide better results. For example, if the flow is stratified or annular, a simpler reconstruction algorithm such as LBP or TR can be used to obtain robust quantitative results in an expedite fashion. If the flow is more complicated, a more sophisticated iterative algorithm might be necessary. To obtain such a priori information, Zhang et al. [68] proposed an ML algorithm based on the support vector machine (SVM) to classify two-phase oil-gas flow patterns. They trained and tested their work for stratified, annular, and core type flows and were able to achieve acceptable accuracy in demonstrating the robustness of their ML-based flow classification algorithm.

9.2. ML-Based Image Reconstruction

As noted before, ECT image reconstruction is challenging due to the non-linearity and ill-posed nature of the inverse problem. In previous sections, we discussed several direct and iterative methods developed to improve ECVT image reconstruction [22]. However, most of these approaches have some limitations. Even in the best-case scenario, the reconstruction resolution is limited by the location in the VoI and several other factors. Recent advances in deep neural networks (DNN) and hardware have revolutionized the use of machine learning to solve many scientific problems, including ECT/ECVT image reconstruction. In the following, we provide a summary review of ML-based image reconstruction efforts tailored to ECT/ECVT sensors.

9.2.1. ECT Image Reconstruction Using Neural Networks

An early ML-based ECT image reconstruction algorithm was proposed by Marashdeh et al. [69] using a multilayer feed-forward neural network combined with an analog Hopfield field network to solve the non-linear inverse problem. The results demonstrated superiority in terms of both stability and quality of reconstructed images versus conventional techniques. Another ML-based approach [70] employed modular deep neural networks to decompose the imaging domain into sub-domains, each having a dedicated sub-neural network to perform the inverse problem.

9.2.2. LSSVM-Based Image Reconstruction

Chen et al. [71] and Wang et al. [72] have both proposed ECT image reconstruction algorithms based on the least squares support vector machine (LSSVM). Chen et al. combined the LSSVM with a self-adaptive particle swarm optimization algorithm to enhance imaging results, and Wang et al. combined the LSSVM with bacterial colony chemotaxis (BCC) algorithm to improve multiphase flow monitoring. Experimental and simulation-based results show that both these approaches are promising; however, the results are strongly dependent on the proper SVM kernel parameter choice.

9.2.3. RBF-NN Based Image Reconstruction

A radial basis function (RBF) neural network combined with adaptive wavelet image enhancement was proposed in [73] to improve ECT image reconstruction. To achieve desired results, a three-layer feed-forward NN (one input, one output, and one hidden layer) with RBF activation was first used to map the pixel to measured capacitance, and consequently obtained the permittivity distribution from the measured capacitance data. After obtaining the first-pass reconstructed images, an adaptive wavelet enhancement technique was applied to improve image quality. Although the results in [73] are good, a traditional ECT algorithm such as ILM can be optimized to obtain similar results for the considered flow type.

9.2.4. Auto-Encoder Image Reconstruction

Two ECT image reconstruction approaches based on auto-encoder ML algorithms were recently presented in [74–76]. The first method [74] is based on a fully connected auto-encoder-based NN algorithm. The second method [76] utilizes a CNN-based auto-encoder algorithm. The proposed fully connected auto-encoder has a total of eight layers: four layers for the encoder and four layers for the decoder part of the network. The CNN auto-encoder uses some CNN layers with max-pooling for the encoder network, and the decoder network has an upsampling layer with few CNN layers. In both cases, the input of the encoder and output of the decoder network correspond to the true and estimated image distribution, respectively; and the output of the encoder and input of the decoder network correspond to the estimated and measured capacitance data, respectively. In both auto-encoders, a ReLU activation function is used for the hidden layers and a sigmoid function for the output layers. The objective of such algorithms is to train the encoder to estimate the measured capacitance and consequently train the decoder network to estimate

the image distribution. Training of the encoder and decoder is carried out simultaneously, and as such, the encoder and decoder networks can be considered as a single autoencoder model [74,76]. Although the preliminary results presented in these works are promising, their appropriateness to real-life ECT/ECVT sensor applications remains to be determined.

9.2.5. Deep-Learning-Compensated Image Reconstruction Algorithms

Most of the previously proposed ML-based image reconstruction algorithms employ a data-driven approach for ECT image reconstruction, whereby the images are obtained directly based on the measured capacitance data. In contrast, a recent work by Zheng et al. [77] proposed a deep-learning-compensated back-projection algorithm to post-process and enhance the image quality obtained from the LBP algorithm. In their work, the authors utilized a CNN-based decoder network to estimate the image reconstruction error of LBP images and consequently improved the imaging quality by a correction procedure. The proposed encoder has six layers, with four hidden layers. The input of the network is the difference between the measured capacitance and estimated capacitance obtained from the LBP algorithm. The output of the network is the imaging error that can be used to compensate for reconstruction results obtained from LBP. Although the results are promising compared to LBP images, the overall results are not markedly superior to the existing iterative algorithm.

9.2.6. Adversarial ML Models for Based Image Reconstruction

The recent work by Deab et al. [78] utilizes a conditional adversarial ML algorithm to improve the image resolution of ECT images. The proposed model consists of a UNet-based generator and a discriminator. The generator consists of eight layers, four layers for the encoder and four layers for the decoder. Discriminator details are unclear. The generator is used to obtain high-resolution images from low-resolution images obtained after the first iteration of the ILM algorithm. The discriminator is then used in the training process to improve the reconstruction results of the generator. The proposed model was trained using a large set of simulation data and was validated using both simulation data (not utilized in the training) and experimental data. The results presented in the paper seem to be superior to those of other existing ML-based ECT algorithms, but additional comparative results are needed to assess the strengths of the adversarial ML approach in industrial ECT/ECVT settings.

9.2.7. Relevance Vector Machine (RVM) and Uncertainty Quantification

In many industrial applications, it is of great interest to provide, along with the reconstructed image of the flow, uncertainty estimates thereof. Such estimates seek to measure the degree of confidence in the imaging results provided. This objective can be accomplished by means of a Bayesian formulation of the inverse problem whereby the solution is expressed in terms of a probability density function, the mean value of which can be identified as the reconstructed image and the variance as a measure of uncertainty in the image. A Relevance Vector Machine (RVM) is an ML-based Bayesian approach that can be used to provide such types of probabilistic solutions. A successful application of RVM to the ECT imaging problem was demonstrated in [57], where a connection between the reconstructed pixel values and the corresponding uncertainty estimates was obtained. The work in [57] showed that, in addition to the key advantage of providing uncertainty measures, RVM-based image reconstruction can achieve a similar resolution as ILM and the least absolute shrinkage and selection operator (LASSO) in typical ECT scenarios, but with less or similar computational complexity. The RVM algorithm was later also utilized to provide an efficient synthetic electrode selection strategy for application in AECVT [79]. The proposed selection strategy was based on the Adaptive Relevance Vector Machine (ARVM) method and allowed the determination of synthetic electrode configurations that yielded the greatest decrease in the image reconstruction uncertainty. By using ARVM,

good image reconstruction and low uncertainty levels can be achieved with considerably fewer AECVT measurements (and hence faster overall acquisition speed).

10. Conclusions and Look Ahead

Accurate monitoring of multiphase flows is becoming a crucial element in the energy industry. Among the available measurement modalities, ECVT has attracted much attention due to its low cost and flexibility. Although ECVT is robust in monitoring multiphase flows, several challenges still remain, such as monitoring water-dominated flows, accurate calculation of flow velocity, and improving image reconstruction resolution. Recent advances in multi-frequency ECVT exploiting the MWS effect have enabled the development of several novel methods to monitor water-containing flows. Moreover, a newly developed and related tomographic modality DCPT, which maps the small-angle perturbation of the measured admittance data to the conductivity distribution in the VoI, has further improved the potential for monitoring of water-containing flows using ECVT sensor technology.

Apart from developing novel methods with which to monitor water-containing flows, recent studies have also focused on developing technologies such as AECVT and cross-plane acquisition to improve the imaging resolution of ECVT. However, the typical image reconstruction resolution of ECVT remains limited, and much work is still needed to improve it. Recent advances in hardware and machine learning have ushered in new possibilities toward this objective. Some of the latest work published in the last few years [74,76,78] suggests improved image reconstruction performance provided by ML-based algorithms applied to ECT/ECVT. Additionally, a properly trained model can also image geometries that were previously considered almost unfeasible due to the nonlinear nature of the ECT/ECVT inverse problem.

Nevertheless, ML-based approaches still have some limitations when applied to practical industrial settings that require further investigation. For example, most of the recent ML-based ECT reconstruction algorithms assume a binary permittivity distribution in the VoI and do not provide a solution for multiphase flows containing more than two phases. Current ML-based algorithms also assume flow invariance in the axial direction. In practice, multiphase flows are dynamic phenomena, and the flow invariance assumption in the axial direction can lead to wrong results if the model is overfitted to a flow invariant setup. Therefore, future work in ML-based algorithms should focus on developing ML algorithms that are not limited to binary flow types and can handle variance in the axial direction. Related to this, most ML-based ECT reconstruction algorithms to date have been developed to reconstruct 2D images on a cross-section of the flow. It is highly desirable to develop ML-based algorithms tailored to ECVT (volumetric) image reconstruction.

Author Contributions: Conceptualization: R.K.R., F.L.T. and Q.M.M.; methodology: R.K.R.; software development: R.K.R.; formal analysis: R.K.R., S.M.C. and F.L.T.; investigation: R.K.R.; data curation: R.K.R.; writing—original draft preparation: R.K.R.; writing—revision and editing: R.K.R., S.M.C. and F.L.T.; project administration, F.L.T. and Q.M.M.; funding acquisition, F.L.T. and Q.M.M. All authors have read and agreed to the published version of the manuscript.

Funding: This work was supported in part by the U.S. Department of Energy cooperative agreement DE-FE0031858.

Institutional Review Board Statement: Not applicable.

Informed Consent Statement: Not applicable.

Data Availability Statement: Not applicable.

Conflicts of Interest: The authors declare no conflict of interest.

Abbreviations

The following are the most common abbreviations used in this manuscript:

ECT	Electrical Capacitance Tomography
ECVT	Electrical Capacitance Volume Tomography
AECVT	Adaptive Electrical Capacitance Volume Tomography
DCPT	Displacement Current Phase Tomography
MWS	Maxwell-Wagner-Sillars
Vol	Volume of Interest
LBP	Linear Back Projection
TR	Tikhonov Regularization
ITR	Iterative Tikhonov Regularization
ILM	Iterative Landweber Method
ML	Machine Learning
CNN	Convolutional Neural Network
DNN	Deep Neural Network
LSSVM	Least Square Support Vector Machine
RBF	Radial Basis Function
RVM	Relevance Vector Machine

References

1. Fan, L.S. *Gas-Liquid-Solid Fluidization Engineering*; Butterworth-Heinemann: Boston, MA, USA, 1989. [\[CrossRef\]](#)
2. Han, C.D. Multiphase flow in polymer processing. In *Rheology*; Springer: Berlin/Heidelberg, Germany, 1980; pp. 121–128.
3. Khodakov, A.Y.; Chu, W.; Fongarland, P. Advances in the development of novel cobalt Fischer-Tropsch catalysts for synthesis of long-chain hydrocarbons and clean fuels. *Chem. Rev.* **2007**, *107*, 1692–1744. [\[CrossRef\]](#) [\[PubMed\]](#)
4. Awaleh, M.O.; Soubaneh, Y.D. Waste water treatment in chemical industries: The concept and current technologies. *Hydrol. Curr. Res.* **2014**, *5*, 1.
5. Weber, J.M.; Mei, J.S. Bubbling fluidized bed characterization using Electrical Capacitance Volume Tomography (ECVT). *Powder Technol.* **2013**, *242*, 40–50. [\[CrossRef\]](#)
6. Nadeem, H.; Heindel, T.J. Review of noninvasive methods to characterize granular mixing. *Powder Technol.* **2018**, *332*, 331–350. [\[CrossRef\]](#)
7. Perera, K.; Pradeep, C.; Mylvaganam, S.; Time, R.W. Imaging of oil-water flow patterns by Electrical Capacitance Tomography. *Flow Meas. Instrum.* **2017**, *56*, 23–34. [\[CrossRef\]](#)
8. Guo, Q.; Meng, S.; Wang, D.; Zhao, Y.; Ye, M.; Yang, W.; Liu, Z. Investigation of gas–solid bubbling fluidized beds using ECT with a modified Tikhonov regularization technique. *AIChE J.* **2018**, *64*, 29–41. [\[CrossRef\]](#)
9. Warsito, W.; Marashdeh, Q.; Fan, L.S. Electrical Capacitance Volume Tomography. *IEEE Sens. J.* **2007**, *7*, 525–535. [\[CrossRef\]](#)
10. Wang, A.; Marashdeh, Q.M.; Teixeira, F.L.; Fan, L.S. Electrical capacitance volume tomography: A comparison between 12 and 24-channels sensor systems. *Prog. Electromagn. Res.* **2015**, *41*, 73–84. [\[CrossRef\]](#)
11. Wang, A.; Marashdeh, Q.; Motil, B.J.; Fan, L.S. Electrical capacitance volume tomography for imaging of pulsating flows in a trickle bed. *Chem. Eng. Sci.* **2014**, *119*, 77–87. [\[CrossRef\]](#)
12. Alme, K.J.; Mylvaganam, S. Electrical Capacitance Tomography–Sensor Models, Design, Simulations, and Experimental Verification. *IEEE Sens. J.* **2006**, *6*, 1256–1266. [\[CrossRef\]](#)
13. Li, Y.; Yang, W.; Xie, C.G.; Huang, S.; Wu, Z.; Tsamakidis, D.; Lenn, C. Gas/oil/water flow measurement by electrical capacitance tomography. *Meas. Sci. Technol.* **2013**, *24*, 074001. [\[CrossRef\]](#)
14. Liao, A.; Zhou, Q. Application of ECT and relative change ratio of capacitances in probing anomalous objects in water. *Flow Meas. Instrum.* **2015**, *45*, 7–17. [\[CrossRef\]](#)
15. Li, Y.; Holland, D.J. Optimizing the geometry of three-dimensional electrical capacitance tomography sensors. *IEEE Sens. J.* **2015**, *15*, 1567–1574. [\[CrossRef\]](#)
16. Marashdeh, Q.M.; Teixeira, F.L.; Fan, L.S. Electrical capacitance tomography. In *Industrial Tomography*; Wang, M., Ed.; Woodhead/Elsevier: Cambridge, UK, 2015; pp. 3–21.
17. Xie, C.; Huang, S.; Beck, M.; Hoyle, B.; Thorn, R.; Lenn, C.; Snowden, D. Electrical capacitance tomography for flow imaging: System model for development of image reconstruction algorithms and design of primary sensors. *IEE Proc. G (Circuits Devices Syst.)* **1992**, *139*, 89–98. [\[CrossRef\]](#)
18. Huang, S.; Xie, C.; Salkeld, J.; Plaskowski, A.; Thorn, R.; Williams, R.; Hunt, A.; Beck, M. Process tomography for identification, design and measurement in industrial systems. *Powder Technol.* **1992**, *69*, 85–92. [\[CrossRef\]](#)
19. Yang, W.; Beck, M.; Byars, M. Electrical capacitance tomography—From design to applications. *Meas. Control* **1995**, *28*, 261–266. [\[CrossRef\]](#)
20. Williams, R.A.; Beck, M.S. *Process Tomography*; Butterworth-Heinemann: Oxford, UK, 1995. [\[CrossRef\]](#)

21. Dyakowski, T.; Edwards, R.; Xie, C.; Williams, R.A. Application of capacitance tomography to gas-solid flows. *Chem. Eng. Sci.* **1997**, *52*, 2099–2110. [[CrossRef](#)]
22. Yang, W.Q.; Peng, L. Image reconstruction algorithms for electrical capacitance tomography. *Meas. Sci. Technol.* **2003**, *14*, R1. [[CrossRef](#)]
23. Watzenig, D.; Fox, C. A review of statistical modelling and inference for electrical capacitance tomography. *Meas. Sci. Technol.* **2009**, *20*, 052002. [[CrossRef](#)]
24. Marashdeh, Q.; Teixeira, F.L. Sensitivity matrix calculation for fast 3-D electrical capacitance tomography (ECT) of flow systems. *IEEE Trans. Magn.* **2004**, *40*, 1204–1207. [[CrossRef](#)]
25. Kim, Y.S.; Lee, S.H.; Ijaz, U.Z.; Kim, K.Y.; Choi, B.Y. Sensitivity map generation in electrical capacitance tomography using mixed normalization models. *Meas. Sci. Technol.* **2007**, *18*, 2092. [[CrossRef](#)]
26. Guo, Z.; Shao, F.; Lv, D. Sensitivity matrix construction for electrical capacitance tomography based on the difference model. *Flow Meas. Instrum.* **2009**, *20*, 95–102. [[CrossRef](#)]
27. Lu, G.; Peng, L.; Zhang, B.; Liao, Y. Preconditioned Landweber iteration algorithm for electrical capacitance tomography. *Flow Meas. Instrum.* **2005**, *16*, 163–167. [[CrossRef](#)]
28. Li, Y.; Yang, W. Image reconstruction by nonlinear Landweber iteration for complicated distributions. *Meas. Sci. Technol.* **2008**, *19*, 094014. [[CrossRef](#)]
29. Jang, J.D.; Lee, S.H.; Kim, K.Y.; Choi, B.Y. Modified iterative Landweber method in electrical capacitance tomography. *Meas. Sci. Technol.* **2006**, *17*, 1909. [[CrossRef](#)]
30. Yang, W.Q.; Spink, D.M.; York, T.A.; McCann, H. An image-reconstruction algorithm based on Landweber's iteration method for electrical-capacitance tomography. *Meas. Sci. Technol.* **1999**, *10*, 1065–1069. [[CrossRef](#)]
31. Ye, J.; Wang, H.; Yang, W. Image Reconstruction for Electrical Capacitance Tomography Based on Sparse Representation. *IEEE Trans. Instrum. Meas.* **2015**, *64*, 89–102. [[CrossRef](#)]
32. de Moura, H.L.; Pipa, D.R.; Wrasse, A.d.N.; da Silva, M.J. Image Reconstruction for Electrical Capacitance Tomography Through Redundant Sensitivity Matrix. *IEEE Sens. J.* **2017**, *17*, 8157–8165. [[CrossRef](#)]
33. Soleimani, M.; Lionheart, W.R. Nonlinear image reconstruction for electrical capacitance tomography using experimental data. *Meas. Sci. Technol.* **2005**, *16*, 1987. [[CrossRef](#)]
34. Marashdeh, Q.; Warsito, W.; Fan, L.S.; Teixeira, F.L. A Multimodal Tomography System Based on ECT Sensors. *IEEE Sens. J.* **2007**, *7*, 426–433. [[CrossRef](#)]
35. Marashdeh, Q.; Warsito, W.; Fan, L.S.; Teixeira, F.L. Dual imaging modality of granular flow based on ECT sensors. *Granul. Matter* **2008**, *10*, 75–80. [[CrossRef](#)]
36. Zhang, M.; Soleimani, M. Simultaneous reconstruction of permittivity and conductivity using multi-frequency admittance measurement in electrical capacitance tomography. *Meas. Sci. Technol.* **2016**, *27*, 025405. [[CrossRef](#)]
37. Gunes, C.; Marashdeh, Q.; Teixeira, F. A Comparison Between Electrical Capacitance Tomography and Displacement-Current Phase Tomography. *IEEE Sens. J.* **2017**, *17*, 8037–8046. [[CrossRef](#)]
38. Rasel, R.K.; Zuccarelli, C.; Marashdeh, Q.; Fan, L.S.; Teixeira, F.L. Towards Multiphase Flow Decomposition Based on Electrical Capacitance Tomography Sensors. *IEEE Sens. J.* **2017**, *17*, 8027–8036. [[CrossRef](#)]
39. Rasel, R.K.; Marashdeh, Q.; Teixeira, F.L. Toward Electrical Capacitance Tomography of Water-Dominated Multiphase Vertical Flows. *IEEE Sens. J.* **2018**, *18*, 10041–10048. [[CrossRef](#)]
40. Becher, P. *Dielectric Properties of Emulsions and Related Systems, Encyclopedia of Emulsion Technology*; M. Dekker: New York, NY, USA, 1983.
41. Maxwell, J.C. *A Treatise on Electricity and Magnetism*; Clarendon: Oxford, UK, 1892.
42. Wagner, K.W. The after effect in dielectrics. *Arch. Electrotech.* **1914**, *2*, 378.
43. Sillars, R. The properties of a dielectric containing semiconducting particles of various shapes. *Inst. Electr. Eng. Proc. Wirel. Sect. Inst.* **1937**, *12*, 378–394.
44. Sihvola, A.H.; Lindell, I.V. Chiral Maxwell-Garnett mixing formula. *Electron. Lett.* **1990**, *26*, 118–119. [[CrossRef](#)]
45. Hanai, T. Theory of the dielectric dispersion due to the interfacial polarization and its application to emulsions. *Kolloid-Zeitschrift* **1960**, *171*, 23–31. [[CrossRef](#)]
46. Hossain, M.S.; Abir, M.T.; Alam, M.S.; Volakis, J.L.; Islam, M.A. An Algorithm to Image Individual Phase Fractions of Multiphase Flows Using Electrical Capacitance Tomography. *IEEE Sens. J.* **2020**, *20*, 14924–14931. [[CrossRef](#)]
47. Rasel, R.K.; Straiton, B.; Marashdeh, Q.; Teixeira, F.L. Toward Water Volume Fraction Calculation in Multiphase Flows Using Electrical Capacitance Tomography Sensors. *IEEE Sens. J.* **2020**, *21*, 7702–7712. [[CrossRef](#)]
48. Rasel, R.K.; Straiton, B.J.; Solon, A.; Marashdeh, Q.M.; Teixeira, F.L. Deep Learning Based Volume Fraction Estimation for Two-Phase Water-Containing Flows. In Proceedings of the 2021 IEEE Sensors, Sydney, Australia, 31 October–3 November 2021; pp. 1–4. [[CrossRef](#)]
49. Rasel, R.K.; Gunes, C.; Marashdeh, Q.M.; Teixeira, F.L. Exploiting the Maxwell-Wagner-Sillars Effect for Displacement-Current Phase Tomography of Two-Phase Flows. *IEEE Sens. J.* **2017**, *17*, 7317–7324. [[CrossRef](#)]
50. Ospina Acero, D.; Chowdhury, S.M.; Marashdeh, Q.M.; Teixeira, F.L. Efficient and Flexible Sensitivity Matrix Computation for Adaptive Electrical Capacitance Volume Tomography. *IEEE Trans. Instrum. Meas.* **2021**, *70*, 1–10. [[CrossRef](#)]

51. Chowdhury, S.M.; Marashdeh, Q.M.; Teixeira, F.L. Electronic Scanning Strategies in Adaptive Electrical Capacitance Volume Tomography: Tradeoffs and Prospects. *IEEE Sens. J.* **2020**, *20*, 9253–9264. [[CrossRef](#)]
52. Zeeshan, Z.; Zuccarelli, C.E.; Acero, D.O.; Marashdeh, Q.M.; Teixeira, F.L. Enhancing Resolution of Electrical Capacitive Sensors for Multiphase Flows by Fine-Stepped Electronic Scanning of Synthetic Electrodes. *IEEE Trans. Instrum. Meas.* **2019**, *68*, 462–473. [[CrossRef](#)]
53. Marashdeh, Q.M.; Teixeira, F.L.; Fan, L.S. Adaptive electrical capacitance volume tomography. *IEEE Sens. J.* **2014**, *14*, 1253–1259. [[CrossRef](#)]
54. Zeeshan, Z.; Teixeira, F.; Marashdeh, Q. Sensitivity map computation in adaptive electrical capacitance volume tomography with multielectrode excitations. *Electron. Lett.* **2015**, *51*, 334–336. [[CrossRef](#)]
55. Zhao, J.; Zou, X.; Fu, W. Sensitivity map analysis of adaptive electrical capacitance volume tomography using nonuniform voltage excitation envelopes. *IEEE Sens. J.* **2017**, *17*, 105–112. [[CrossRef](#)]
56. Song, P.; Zhao, J.; Fu, W.; Xia, T. Image reconstruction in adaptive electrical capacitance volume tomography using nonuniform voltage excitation envelopes. In Proceedings of the 2017 3rd IEEE International Conference on Computer and Communications (ICCC), Chengdu, China, 13–16 December 2017; pp. 1907–1911. [[CrossRef](#)]
57. Ospina-Acero, D.; Marashdeh, Q.M.; Teixeira, F.L. Relevance Vector Machine Image Reconstruction Algorithm for Electrical Capacitance Tomography With Explicit Uncertainty Estimates. *IEEE Sens. J.* **2020**, *20*, 4925–4939. [[CrossRef](#)]
58. Rasel, R.K.; Sines, J.N.; Marashdeh, Q.; Teixeira, F.L. Cross-plane acquisitions in electrical capacitance volume tomography. *IEEE Sens. J.* **2019**, *19*, 8767–8774. [[CrossRef](#)]
59. Li, Y.; Holland, D.J. Fast and robust 3D electrical capacitance tomography. *Meas. Sci. Technol.* **2013**, *24*, 105406. [[CrossRef](#)]
60. Saoud, A.; Mosorov, V.; Grudzien, K. Measurement of velocity of gas/solid swirl flow using Electrical Capacitance Tomography and cross correlation technique. *Flow Meas. Instrum.* **2017**, *53*, 133–140. [[CrossRef](#)]
61. Yang, W. Design of electrical capacitance tomography sensors. *Meas. Sci. Technol.* **2010**, *21*, 042001. [[CrossRef](#)]
62. Warsito, W.; Fan, L.S. 3D-ECT velocimetry for flow structure quantification of gas-liquid–solid fluidized beds. *Can. J. Chem. Eng.* **2003**, *81*, 875–884. [[CrossRef](#)]
63. Botton, L.F.; de Moura, H.L.; Wrasse, A.N.; Pipa, D.R.; Morales, R.E.; da Silva, M.J. Twin Direct-Imaging Sensor for Flow Velocity Profiling in Two-Phase Mixtures. In Proceedings of the 2018 IEEE Sensors, New Delhi, India, 28–31 October 2018; pp. 1–4.
64. Chowdhury, S.; Marashdeh, Q.M.; Teixeira, F.L. Velocity Profiling of Multiphase Flows Using Capacitive Sensor Sensitivity Gradient. *IEEE Sens. J.* **2016**, *16*, 8365–8373. [[CrossRef](#)]
65. Park, C.; Chowdhury, S.M.; Pottimurthy, Y.; Marashdeh, Q.M.; Tong, A.; Teixeira, F.L.; Fan, L.S. Velocity profiling of a gas-solid fluidized bed using electrical capacitance volume tomography. *IEEE Trans. Instrum. Meas.* **2022**, *accepted*. [[CrossRef](#)]
66. Chowdhury, S.M.; Park, C.; Pottimurthy, Y.; Marashdeh, Q.M.; Teixeira, F.L.; Fan, L.S. Robust Automated Stopping Criterion for Semi-Convergent Image and Velocity Reconstruction in Electrical Capacitance Volume Tomography. *IEEE Open J. Instrum. Meas.* **2022**, *in review*.
67. Gunes, C.; Chowdhury, S.M.; Zuccarelli, C.E.; Marashdeh, Q.M.; Teixeira, F.L. Displacement-current phase tomography for water-dominated two-phase flow velocimetry. *IEEE Sens. J.* **2018**, *19*, 1563–1571. [[CrossRef](#)]
68. Zhang, L.; Wang, H. Identification of oil–Gas two-phase flow pattern based on SVM and electrical capacitance tomography technique. *Flow Meas. Instrum.* **2010**, *21*, 20–24. [[CrossRef](#)]
69. Marashdeh, Q.; Warsito, W.; Fan, L.S.; Teixeira, F.L. A nonlinear image reconstruction technique for ECT using a combined neural network approach. *Meas. Sci. Technol.* **2006**, *17*, 2097. [[CrossRef](#)]
70. Chen, E.; Sarris, C.D. A Multi-Level Reconstruction Algorithm for Electrical Capacitance Tomography Based on Modular Deep Neural Networks. In Proceedings of the 2019 IEEE International Symposium on Antennas and Propagation and USNC-URSI Radio Science Meeting, Atlanta, GA, USA, 7–12 July 2019; pp. 223–224. [[CrossRef](#)]
71. Chen, X.; Hu, H.I.; Liu, F.; Gao, X.X. Image reconstruction for an electrical capacitance tomography system based on a least-squares support vector machine and a self-adaptive particle swarm optimization algorithm. *Meas. Sci. Technol.* **2011**, *22*, 104008. [[CrossRef](#)]
72. Wang, H.; Hu, H.I.; Wang, L.j.; Wang, H.x. Image reconstruction for an Electrical Capacitance Tomography (ECT) system based on a least squares support vector machine and bacterial colony chemotaxis algorithm. *Flow Meas. Instrum.* **2012**, *27*, 59–66. [[CrossRef](#)]
73. Xia, C.; Hongli, H.; ZHANG, J.; Qulan, Z. An ECT system based on improved RBF network and adaptive wavelet image enhancement for solid/gas two-phase flow. *Chin. J. Chem. Eng.* **2012**, *20*, 359–367.
74. Zheng, J.; Peng, L. An autoencoder-based image reconstruction for electrical capacitance tomography. *IEEE Sens. J.* **2018**, *18*, 5464–5474. [[CrossRef](#)]
75. Zheng, J.; Li, J.; Li, Y.; Peng, L. A benchmark dataset and deep learning-based image reconstruction for electrical capacitance tomography. *Sensors* **2018**, *18*, 3701. [[CrossRef](#)] [[PubMed](#)]
76. Zheng, J.; Ma, H.; Peng, L. A CNN-based image reconstruction for electrical capacitance tomography. In Proceedings of the 2019 IEEE International Conference on Imaging Systems and Techniques (IST), Abu Dhabi, United Arab Emirates, 9–10 December 2019; pp. 1–6.
77. Zheng, J.; Peng, L. A deep learning compensated back projection for image reconstruction of electrical capacitance tomography. *IEEE Sens. J.* **2020**, *20*, 4879–4890. [[CrossRef](#)]

-
78. Deabes, W.; Abdel-Hakim, A.E.; Bouazza, K.E.; Althobaiti, H. Adversarial Resolution Enhancement for Electrical Capacitance Tomography Image Reconstruction. *Sensors* **2022**, *22*, 3142. [[CrossRef](#)]
 79. Acero, D.O.; Marashdeh, Q.M.; Teixeira, F.L. Reduced-Space Relevance Vector Machine for Adaptive Electrical Capacitance Volume Tomography. *IEEE Trans. Comput. Imaging* **2022**, *8*, 41–53. [[CrossRef](#)]